

Environmental memory boosts group formation of clueless individuals

Received: 12 June 2023

Accepted: 31 October 2023

Published online: 13 November 2023

 Check for updates

Cristóvão S. Dias^{1,2}, Manish Trivedi³, Giovanni Volpe⁴✉, Nuno A. M. Araújo^{1,2}✉ & Giorgio Volpe³✉

The formation of groups of interacting individuals improves performance and fitness in many decentralised systems, from micro-organisms to social insects, from robotic swarms to artificial intelligence algorithms. Often, group formation and high-level coordination in these systems emerge from individuals with limited information-processing capabilities implementing low-level rules of communication to signal to each other. Here, we show that, even in a community of clueless individuals incapable of processing information and communicating, a dynamic environment can coordinate group formation by transiently storing memory of the earlier passage of individuals. Our results identify a new mechanism of indirect coordination via shared memory that is primarily promoted and reinforced by dynamic environmental factors, thus overshadowing the need for any form of explicit signalling between individuals. We expect this pathway to group formation to be relevant for understanding and controlling self-organisation and collective decision making in both living and artificial active matter in real-life environments.

Strength in numbers is more than an idiomatic expression. Many living systems form groups to improve their fitness, optimise the use and allocation of resources, and reach consensus¹. Examples emerge at all length scales, from bacterial quorum sensing and biofilm formation² to social insects³, from animal groups⁴ to human crowds⁵. Artificial active matter systems, such as active colloids⁶ and robotic swarms⁷, provide controllable systems to pinpoint the essential principles behind the emergence of these collective behaviours in living systems^{8,9}. For example, active colloids have been employed to demonstrate motility-induced phase separation^{10,11} as well as the spontaneous formation of living crystals resembling animal group formation^{8,12}. Complex dynamic collective patterns, such as colloidal swarms, flocks and swirls, have also been demonstrated by introducing controllable attractive, repulsive or aligning interactions among individuals by particle design^{13,14}, by defining appropriate confining potentials¹⁵ or by modulating particles' propulsion with external feedback loops^{9,16}. In recent years, a few active particles in crowded environments of passive

colloids have also been employed to modulate the energy landscape of the passive phase with an emphasis on controlling the assembly of soft materials^{17–25}.

Whether living or artificial, decentralised systems are characterised by high-level coordination and collective behaviours, which emerge from individuals with limited information-processing capabilities responding to low-level rules of engagement²⁶. In particular, stigmergy is a form of indirect communication between individuals by means of the environment, either mediated by physical modifications (sematectonic stigmergy) or by a signalling mechanism via deposition of markers (marker-based stigmergy) which shape a shared environmental memory²⁷. This strategy underpins the emergence of coordination and collective decision-making in many natural decentralised systems, from micro-organisms² to social insects³. For example, trailing stalk cells guided by chemo-attractants through tissue establish the vascular lumen in sprout angiogenesis²⁸; bacteria²⁹, amoebas³⁰ and ants³¹ can solve physical mazes by tracking chemical scents and

¹Departamento de Física, Faculdade de Ciências, Universidade de Lisboa, 1749-016 Lisboa, Portugal. ²Centro de Física Teórica e Computacional, Faculdade de Ciências, Universidade de Lisboa, 1749-016 Lisboa, Portugal. ³Department of Chemistry, University College London, 20 Gordon Street, WC1H 0AJ London, UK.

⁴Department of Physics, University of Gothenburg, Origovägen 6B, SE-412 96 Gothenburg, Sweden. ✉ e-mail: giovanni.volpe@physics.gu.se; nmaraujo@fc.ul.pt; g.volpe@ucl.ac.uk

forming optimal paths; mutual anticipation and avoidance in crowds lead to lane formation and stabilisation³². The concept of stigmergy has also found widespread use in technological and engineering applications, from robotic swarms³³ to artificial intelligence algorithms⁷, to, recently, active colloids³⁴. In these systems, it is usually assumed that individuals possess a minimal level of low-level communication and signal processing capabilities, which leads to the emergence of shared environmental memory and, eventually, high-level group dynamics²⁷.

Here, we demonstrate that, even in a community of clueless self-motile individuals (i.e., incapable of directly signalling to each other or processing information), avoidance of a dense population of non-fixed obstacles is sufficient to lead to the emergence of stigmergy when the dynamic environment can transiently store memory of the earlier passage of individuals. Counterintuitively, we find that, while the motion of the individuals is hampered by increasing levels of crowding, the spatial correlations created and stored in the otherwise passive environment after their passage feed back on the motion of other individuals to boost aggregation rates and, consequently, group formation.

Results

Group formation experiments

As paradigmatic self-motile individuals, we employ Janus silica (SiO_2) colloids (diameter $d = 4.77 \pm 0.20 \mu\text{m}$) half-coated with a thin layer of carbon ($\approx 60 \text{ nm}$) (Methods). When suspended in a critical binary mixture of water and 2,6-lutidine (0.286 mass fraction of lutidine) below its lower critical temperature ($T_c \approx 307 \text{ K}$), these colloids undergo Brownian diffusion³⁵. Upon exposure to laser illumination ($\lambda = 532 \text{ nm}$, $I \approx 2.5 \mu\text{W} \mu\text{m}^{-2}$) (Methods), light absorption at the carbon cap simultaneously propels the Janus particles in the field of view with the more hydrophobic carbon-coated side at the front at a speed of $v \approx 1.9 \mu\text{m s}^{-1}$ due to local heating and demixing of the critical mixture around the cap³⁵. Our experiments are in the Stokes regime (Reynolds numbers, $\text{Re} \approx 10^{-5} \ll 1$) and inertial effects, including those of the fluid^{36,37}, can be safely neglected. Because of their colloidal nature, these self-motile individuals are clueless in the sense that they have no sensing or information-processing capabilities and interact with each other through simple physical interaction rules, such as steric and short-range attractive interactions^{8,10,38}. Boundaries can also influence their motion with aligning interactions^{39,40}.

To study their interplay with a dynamic environment of non-static obstacles, we prepare quasi-two-dimensional samples of Janus particles mixed with dispersions of equally sized freely diffusing silica (SiO_2) colloids at different densities ($0 \leq \rho_p \leq 75\%$, defined as fractional surface coverage), where the Janus particles only represent a small portion ($0.5\% \leq \rho_a \leq 1.6\%$, also defined as fractional surface coverage) (Methods). The two example time sequences of active particles ($\rho_a = 1.1\%$) moving in a crowded environment ($\rho_p = 37.5\%$) in Fig. 1 and Supplementary Fig. 1 show how the changes introduced in the passive phase by the active colloids produce spatial correlations in the environment in the form of open transient paths. These paths feedback on the motion of the active particles, eventually leading to group formation (here defined as the formation of a cluster of at least three particles separated by at most $0.1d$ from another particle and surviving for at least one frame). While moving forward, individual Janus particles need to physically dig their own path against the surrounding background of passive colloids (Fig. 1a and Supplementary Fig. 1a). Although the presence of voids in the background of passive particles can simplify this task at times, their overall motility reduces for increasing values of ρ_p as exemplified by the mean square displacements (MSDs) in Supplementary Fig. 2. Unless pushed by a Janus particle, the motion dynamics of the passive particles remain diffusive at the edges of the transient paths (Fig. 1a and Supplementary Fig. 1a).

Interestingly, before closing due to the Brownian motion of the passive colloids, these paths appear to be reused by other active colloids, which favour reusing these preformed paths of lower resistance from either end rather than digging their own (Fig. 1b and Supplementary Fig. 1b). A form of stigmergy (consistent with the definition of sematectonic stigmergy²⁷) between the active particles is then established thanks to their passive counterparts, where the transient paths opened by the active colloids in their surroundings become a shared

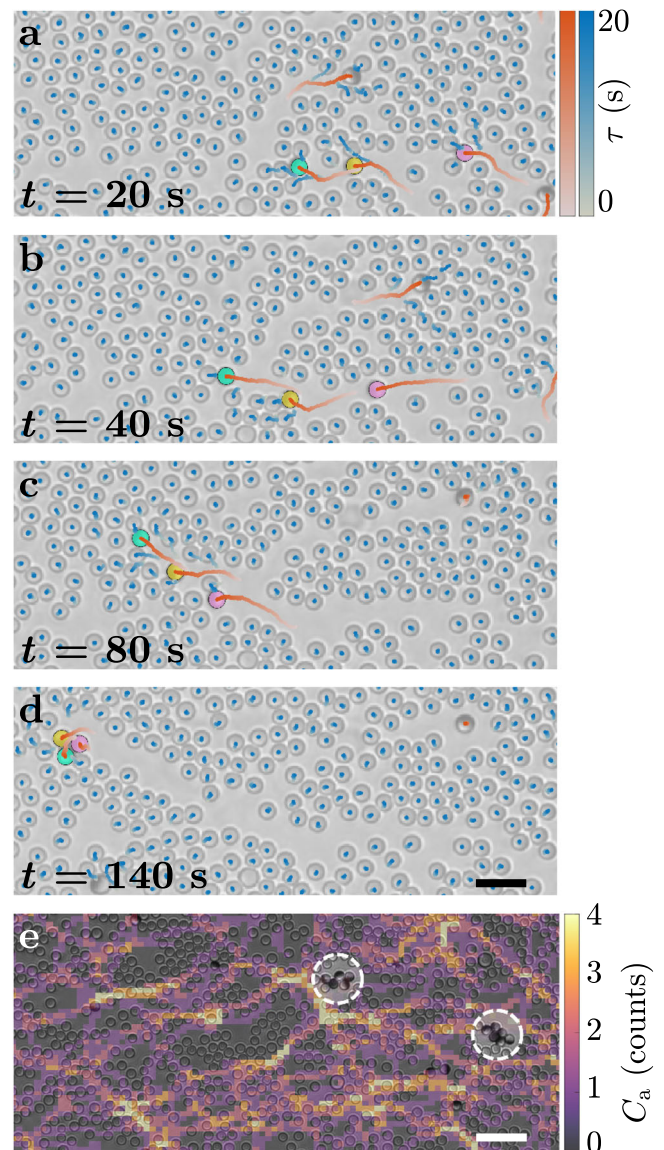


Fig. 1 | Group formation of active colloids mediated by environmental memory. **a–d** Time sequence showing **(a)** a light-activated Janus particle (cyan) forming a path in a crowded environment of SiO_2 passive particles (densities: $\rho_a = 1.1\%$ for active particles and $\rho_p = 37.5\%$ for passive particles), **b, c** which is then reused by nearby Janus particles (yellow and magenta) leading to **(d)** the formation of a group (here, a three-particle cluster). In each image, 20-s-long trajectories are shown for both active (red colour scale) and passive (blue colour scale) particles; t represents the time of each frame and τ the time along each trajectory. Scale bar: $10 \mu\text{m}$. **e** Counts C_a (represented as a heatmap) of individual Janus particles that have transited on a pixel during a 16-min acquisition in a similar crowded environment as in **a–d**. The heatmap is overlaid to the final frame showing how path generation and reuse (bright lines) correlate to group formation and cohesion of active units in time (white dashed circles). The heatmap was obtained from a sample with $\rho_a = 1.1\%$ and $\rho_p = 37.5\%$ and an occupied pixel was only accounted for once for each particle. Scale bar: $25 \mu\text{m}$.

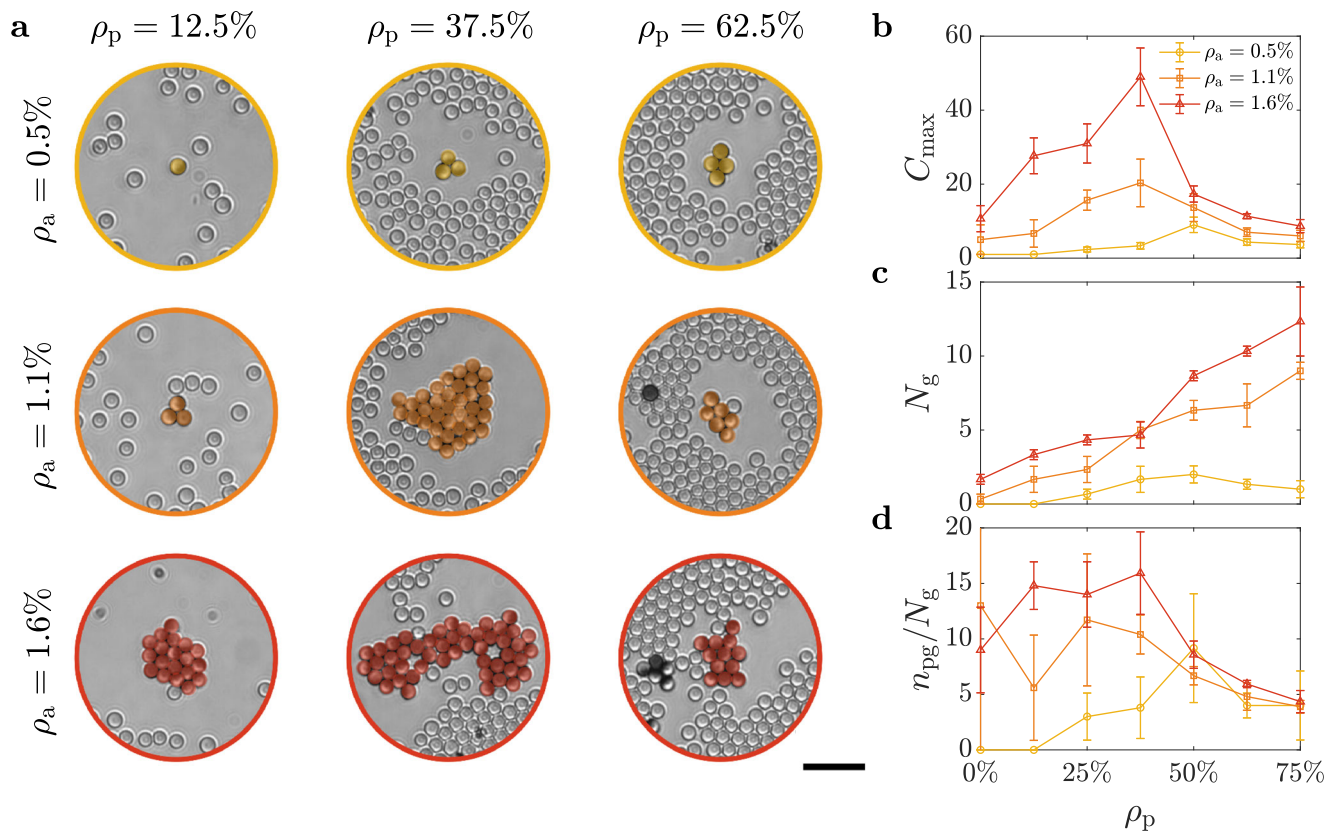


Fig. 2 | Non-monotonic size dependence of group formation on environmental crowding. Groups (here defined as all clusters formed by at least 3 individuals) formed after 25 min as a function of the initial densities of active (ρ_a) and passive (ρ_p) particles. **a** Example images of the largest clusters of active colloids formed at different ρ_a and ρ_p . Independent of ρ_a , these images show how the largest sizes are obtained at intermediate values of ρ_p . Scale bar: 20 μm . **b** This visual trend is confirmed by the non-monotonic dependence of the average size C_{\max} of the largest clusters (measured as number of active particles) as a function of ρ_p for

different values of ρ_a . **c** Differently from C_{\max} , the total number of groups N_g tends to monotonically increase with ρ_p . The error bars in **b** and **c** represent one standard error around the average values obtained from triplicates. **d** Average number of active colloids in a group after 25 min calculated as the ratio between the number of particles in a group n_{pg} and the number of groups N_g . The error bars in **d** are obtained by propagating the standard errors on n_{pg} and N_g . Source data are provided as a Source Data file.

environmental memory for their peers, which generates a feedback that reinforces their trailing behaviour and, eventually, leads to group formation. Indeed, over time, the trailing Janus colloids catch up with the front particles (Fig. 1c and Supplementary Fig. 1c) to form a small cluster (Fig. 1d and Supplementary Fig. 1d). Once formed, these clusters then grow to larger sizes due to the continuous addition of new active particles to the group through a network of similar transient open paths that form and evolve over time (Fig. 1e). As in other cases of sematectonic stigmergy²⁷, therefore, the modifications introduced by the active particles in their physical environment (here, the formation of a path in the background of passive colloids) act as asynchronous cues directing the next steps of other particles (here, changing their direction of motion) in a way that provides a direct contribution to the task (here, the carving, reuse and stabilisation of the paths) and facilitates the emergence of population-level coordination (here, group formation).

Figure 2a shows examples of the largest groups obtained after 25 min of experimental time for different values of ρ_a and ρ_p . Independently of ρ_a , the largest groups appear to form for intermediate values of ρ_p , where the crowding is sufficient to create a shared memory in the environment in the form of reusable transient paths, but not dense enough to completely hamper the motility of the individual Janus particles. To quantify this observation, we calculated the size of the largest cluster C_{\max} (Fig. 2b), the total number of groups N_g (Fig. 2c) and the average number of particles per group (Fig. 2d) for different values of ρ_a as a function of ρ_p . At $\rho_p = 0$, no group forms at a

low density of active particles ($\rho_a = 0.5\%$) as encounters are sparse, while the formation of a very few groups (up to ≈ 2) becomes increasingly more likely for higher values of ρ_a , as chances for encounter increase with the number of available individuals. Increasing ρ_p to intermediate values leads to the formation of more groups on average (for example, up to ≈ 5 at 37.5%, Fig. 2c). The average size of these groups also shows a tendency to increase for a given ρ_a until a peak is reached around intermediate values of ρ_p (Fig. 2d). Both the exact position of this peak and its width depend on ρ_a : the peak is higher, broader, and shifted towards lower values of ρ_p , the higher ρ_a (Fig. 2d). This is also reflected by the trend observed for C_{\max} (Fig. 2b). Indeed, as chances for encounter increase with the number of available active particles, individuals become more efficient at creating and reusing correlations in their environment through the transient paths, thus lowering the density threshold needed for the passive phase to promote group formation with increasing ρ_a . At the peak, a larger cluster tends to emerge (Fig. 2b) that can contain up to $\approx 67\%$ of the particles in a group (n_{pg}) due to the shared environmental memory from the path reuse highlighted in Fig. 1 and Supplementary Fig. 1. This effect is more prominent the higher the value of ρ_a . The path reuse by the Janus particles can be quantified through the path revival function $1 - C_{aa}(\tau)$, where $C_{aa}(\tau)$ is the cumulative probability that a region crossed by an active particle will be crossed by another particle within a lag time τ (Methods). If we consider the particles' velocities to be Poisson distributed when a path is chosen, then this function should follow an exponential distribution for persistent particles of the form

$1 - C_{aa}(\tau) = \exp(-\tau/\tau_{\rho_p})^{41}$, where τ_{ρ_p} is the effective path revival lifetime, which we fit from the data (Supplementary Fig. 3). The shorter τ_{ρ_p} , the faster $1 - C_{aa}(\tau)$ decays (i.e., the faster $C_{aa}(\tau)$ increases to one), the sooner a region explored by a particle will be crossed by another particle, thus indicating a higher likelihood that a previously opened path will be reused by other active particles. Supplementary Fig. 3a shows how, in our experiments, after initial comparable trends at lower values of ρ_p ($\rho_p \leq 25\%$), the decay of the path revival function becomes faster starting from intermediate values of ρ_p (quantified by an approximately factor-two reduction of the path revival lifetime τ_{ρ_p} in Supplementary Fig. 3b), thus indicating a higher likelihood of reusing previously explored regions. This change of the path revival lifetime with ρ_p is unexpected and can only be justified by the emergence of a shared environmental memory due to the reuse of pre-existing paths. In fact, if we consider collisions between persistent particles whose velocities are Poisson distributed⁴¹, we would expect the lifetime of the path revival function τ_{ρ_p} to increase with ρ_p as the particles' effective velocity decreases due to the collisions with the passive particles (as confirmed by the MSDs in Supplementary Fig. 2). Eventually, further increasing ρ_p has a dramatic effect on group formation, as the reduced motility for the active colloids due to the resistance offered by the passive particles (Supplementary Fig. 2) induces a more intuitive behaviour where group formation and cohesion are drastically hampered by the crowded environment and any reduction of the path revival lifetime with respect to the case at $\rho_p = 0\%$ (Supplementary Fig. 3) is now driven by the active particles being more localised in space due to crowding rather than the presence of longer-range correlations in the form of transient paths. For a given ρ_a , the ever-increasing number of groups N_g with ρ_p (Fig. 2c) translates now into smaller groups of more homogeneous sizes and more localised in space, which, differently from N_g , show a milder dependence on the initial value of ρ_a (Fig. 2b, d).

Mechanism behind stigmergy of clueless active colloids

To shed light on the physical mechanism behind the reuse of paths in Fig. 1 and Supplementary Fig. 1, Fig. 3a, b shows a close-up of the motion of a Janus particle in the background of passive particles. At $t = 24$ s (Fig. 3a), the particle approaches a block of relatively packed obstacles. On approaching one of them, it turns clockwise towards a void in the structure formed by the passive colloids instead of pushing ahead. At $t = 34$ s, the Janus particle approaches two obstacles head-on via their middle, thus pushing them out of the way and continuing its journey towards a pre-existing path (Fig. 3b). Interestingly, the particle does not align with this path until it encounters a new block of relatively packed obstacles ($t = 47$ s). At this point, a new reorientation event turns it counter-clockwise, thus aligning the particle's motion to the open path ($t = 58$ s) and allowing its reuse. To interpret these reorientation events, we need to consider how the presence of the obstacles affects the particle's self-propulsion mechanism. In their absence, light absorption at the particle's carbon cap induces the local demixing of the water–2,6-lutidine critical mixture, leading to the formation of a lutidine-rich droplet around the more hydrophobic carbon side and of a smaller water-rich droplet around the more hydrophilic silica side^{35,42}. The formation of these droplets, which propels the particle^{35,42}, is mostly symmetric around the axis defined by the direction of the particle's motion, and the particle's reorientation in a viscous medium is driven by its intrinsic rotational diffusion dynamics^{35,42}. If obstacles are present on one side, the local demixing is no longer symmetric around the direction of the particle's motion. This asymmetry induces a deterministic aligning torque that reorients the particle towards the more demixed side, i.e., eventually away from the obstacles⁴². As can be seen in Fig. 3a, b, this reorientation (and, hence, the presence of the torque) depends on the local configuration of obstacles and continues until the particle is aligned in a direction where the demixing around the caps is symmetric again and the

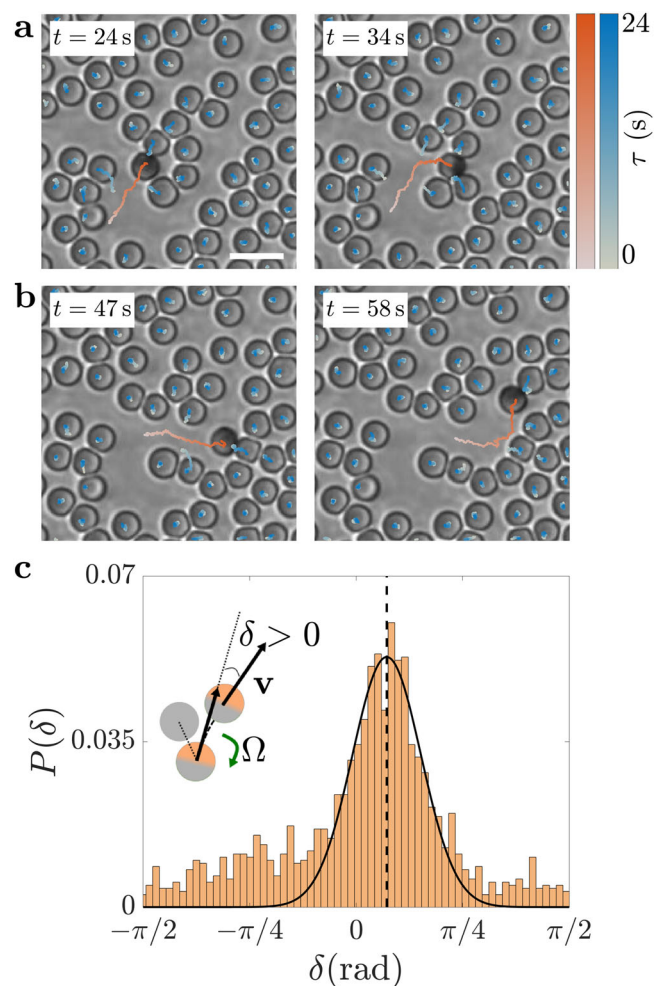


Fig. 3 | Aligning torque as the mechanism for path reuse. a, b Time sequence of a light-activated Janus particle experiencing a torque that aligns it to openings in a crowded environment at a density of SiO_2 passive particles of $\rho_p = 37.5\%$. The effect of this torque on the particle's trajectory is evident in the frames at **a** $t = 34$ s and **b** $t = 58$ s, where the particle has turned clockwise (towards a void in the structure formed by the passive colloids) and counter-clockwise (towards an open path), respectively. In each image, 24-s-long trajectories are shown for both active (red colour scale) and passive (blue colour scale) particles; t represents the time of each frame and τ the time along each trajectory. Scale bar: 10 μm . **c** Probability $P(\delta)$ that a Janus particle moving at a velocity \mathbf{v} is deflected by an angle δ from its direction of approach to an obstacle due to a torque $\mathbf{\Omega}$ (inset). The deflection angle δ is defined between the active particle's direction of approach to the obstacle (at a distance between the two particles' surfaces equal to one diameter d) and its direction of motion after having passed it (after travelling a $2d$ distance); we calculated δ at low density of passive particles ($\rho_p = 12.5\%$) to primarily consider interactions with single obstacles for active particles' approaches within a narrow angular cone ($\pm\pi/8$ excluding near head-on approaches, which contribute symmetrically around $\delta = 0$). Positive δ values indicate deflection away from the obstacles (as shown in the inset), while negative δ values indicate initial deflections towards the obstacles. The solid line is a Gaussian fit (centred at $\delta \approx 0.23$ rad, dashed vertical line) around the position of the peak. Source data are provided as a Source Data file.

aligning torque vanishes (for example, along an open path). To quantify the previous observation, we have calculated the angle δ at which the Janus colloids are deflected by their interaction with the obstacles (Fig. 3c). Positive and negative δ values indicate that the particles are deflected initially away from or towards the obstacles, respectively. When steering away from the obstacles (positive δ), we can then expect the particles to immediately align to openings in the background of passive particles, while deflections towards the obstacles

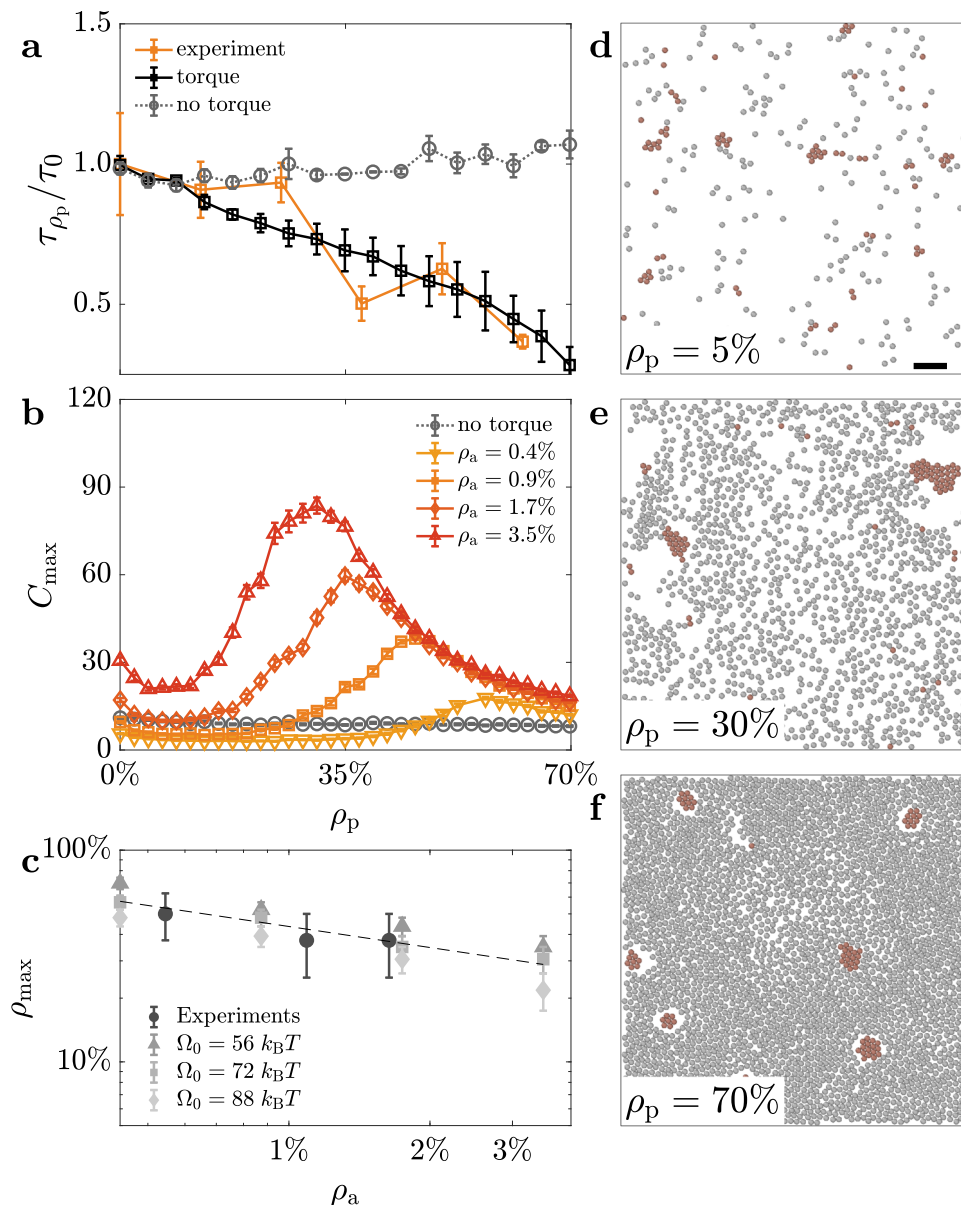


Fig. 4 | Importance of aligning interactions for stigmery of active particles.

a Path revival lifetime τ_{ρ_p} as a function of the density of passive particles ρ_p in experiments for a density of active particles $\rho_a = 1.1\%$ (orange solid line) and in simulations with (black solid line) and without (grey dotted line) an effective aligning torque steering the active particles away from the passive ones. The torque Ω (with strength $\Omega_0 = 72 \pm 16 k_B T$) depends on the local configuration of obstacles (Methods) and is necessary to reproduce the overall experimental trend. The data from Supplementary Fig. 3 are here normalised to τ_0 , the path revival lifetime at $\rho_p = 0$. **b** Simulated average size C_{\max} of the largest group for different ρ_a as a function of ρ_p in the presence (coloured solid lines) and absence (grey dotted line) of an aligning torque, showing that the torque is key to the appearance of a peak at

intermediate values of ρ_p (as in Fig. 2b). **c** The value of ρ_p at the peak position (ρ_{\max}) as a function of ρ_a provides a second estimate for the experimental torque strength ($\Omega_0 = 72 \pm 16 k_B T$). Its monotonously decreasing trend is visualised by a dashed line as a guide for the eyes. Each experimental data point in **a** and **c** is obtained as an average from three videos at the corresponding values of ρ_a and ρ_p and simulations in **a–c** are averages over 100 numerical experiments per value of ρ_a and ρ_p . All error bars represent one standard error around the average values. **d–f** Example snapshots from simulations showing group formation of active particles (red, $\rho_a = 1.1\%$) at different densities of passive particles: **d** $\rho_p = 5\%$, **e** $\rho_p = 30\%$ and **f** $\rho_p = 70\%$. Scale bar: 40 μm . Source data are provided as a Source Data file.

(negative δ) would initially increase chances of collisions with the obstacles until the particle digs a new path or aligns to an existing one. The distribution of angles in Fig. 3c is peaked at positive δ values (as highlighted by the Gaussian fit centred at $\delta \approx 0.23$ rad), thus quantitatively confirming the stronger tendency for active particles to avoid obstacles and align to open paths already on approach.

To gain a microscopic understanding of the non-monotonic dynamics of group formation in Fig. 2b, we can therefore consider a simple particle-based model that includes an aligning torque, which depends on the local configuration of obstacles (Methods)⁴³, in the

equations of motion of the active particles. The effect of this torque is to steer the active particles away from the surrounding passive ones and align their direction of motion to any effective boundary of a transient path^{39,40}. Figure 4a shows how the presence of this aligning torque is already fundamental to reproduce the overall dependence of the experimental path revival lifetime τ_{ρ_p} on ρ_p , indicating that obstacle avoidance is indeed the mechanism that promotes active particles to follow previously formed transient paths. In fact, in the absence of the torque, the path revival lifetime increases with ρ_p as one would intuitively expect due to the decrease of the particles' effective

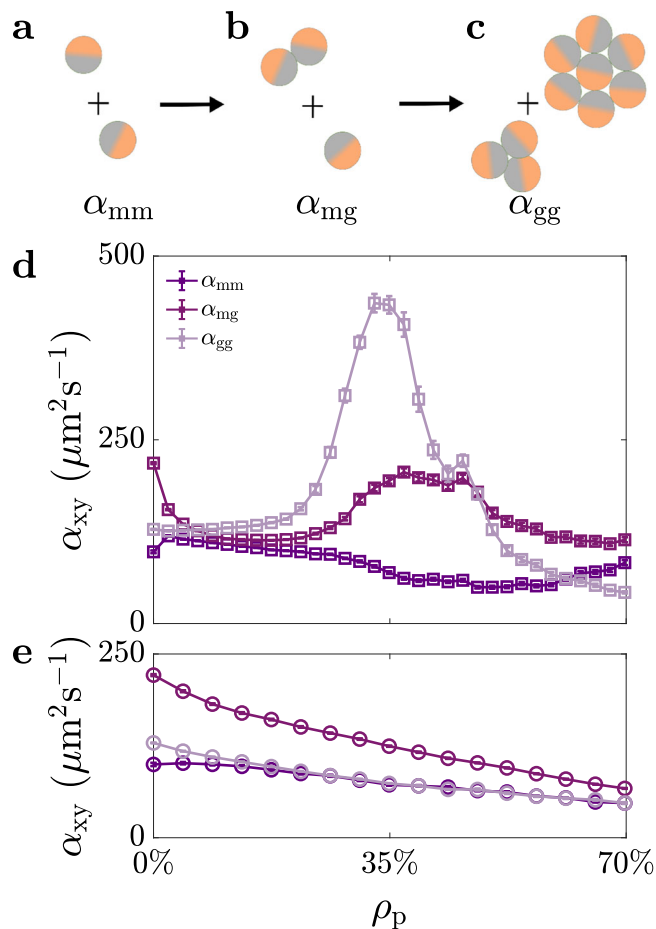


Fig. 5 | Kinetics of group formation with shared environmental memory. **a–c** Schematics of the three main mechanisms for the kinetics of group formation described by the relevant rate coefficients α_{xy} : **a** monomer–monomer (α_{mm}), **b** monomer–group (α_{mg}) and **c** group–group (α_{gg}) aggregation. **d, e** Calculated monomer–monomer (α_{mm}), monomer–group (α_{mg}) and group–group (α_{gg}) aggregation rate coefficients at a density of active particles $\rho_a = 1.1\%$ as a function of the density of passive particles ρ_p (**d**) in the presence of an aligning torque and (**e**) in its absence. Simulations were averaged over 100 numerical experiments per value of ρ_p . Error bars represent one standard error around the average values. Source data are provided as a Source Data file.

velocity caused by collisions with the obstacles⁴¹. Fitting our experimental data to our model allows us to determine the strength of the torque to be $\Omega_0 = 72 \pm 16 k_B T$. As shown in Fig. 4b, the presence of this torque is also critical to recovering the non-monotonic dependence of the largest group size with ρ_p as observed in our experimental data (Fig. 2b). Therefore, this torque and the resulting aligning interaction provide an enabling mechanism for the emergence of stigmergy via a shared environmental memory in the system of non-communicating active particles by allowing the spatial correlations in the environment to feed back on their motion. Figure 4b also confirms that the non-monotonic dynamics of group formation depend on the number of individuals (as already observed in Fig. 2b). At higher values of ρ_a , encounters become more probable so that groups can form and grow to larger sizes at lower values of ρ_p . As groups grow to larger sizes, there is a decrease in the density of passive particles needed to cage them and prevent them from merging into even larger groups. The combination of these two effects translates into a decreasing monotonic dependence of the peak position on ρ_a (Fig. 4c), highlighting the relevance of environmental memory effects for group formation in sparse systems of clueless active particles. Figure 4d–f shows example

snapshots from the simulations, which confirm our qualitative observations in Fig. 2: at low values of ρ_p (Fig. 4d), groups of a few units are formed; at intermediate values of ρ_p (Fig. 4e), the landscape is dominated by a very few large groups that collect most of the active particles; finally, at large values of ρ_p (Fig. 4f), a few relatively smaller groups of more homogeneous size appear to be caged within the crowded environment.

Kinetic model of group formation

To further understand how the shared environmental memory affects encounter dynamics, we can define a kinetic model based on mean-field rate equations for the number density of monomers (free active particles, i.e., not part of a group) c_1 and for the number density of groups c_g as

$$\dot{c}_1 = -\alpha_{mm}c_1^2 - \alpha_{mg}c_1c_g, \quad (1)$$

$$\dot{c}_g = \frac{\alpha_{mm}}{2}c_1^2 - \frac{\alpha_{gg}}{2}c_g^2, \quad (2)$$

where α_{mm} , α_{mg} and α_{gg} are the rate coefficients of monomer–monomer, monomer–group and group–group aggregation (Methods). Rate equations are indeed a powerful tool to understand the emergence of group dynamics and self-assembly in systems of multiple units, as much as in chemical kinetics⁴⁴ and colloidal science¹² as in swarm robotics^{45,46}. In Eq. (1), monomers disappear due to the formation of a new group from two monomers (first term, Fig. 5a) or due to the growth of an existing group by addition of a new monomer (second term, Fig. 5b). Similarly, in Eq. (2), c_g can change due to the formation of a new group from monomers (first term, Fig. 5a) or from the merging of two existing groups (second term, Fig. 5c). In all cases, we assume that the rate of encounters is proportional to the product of the number densities of the species involved (either monomers or groups) and that any dependence on the effective cross-sectional area of each species is accounted for by the effective rates of aggregation α_{mm} , α_{mg} and α_{gg} . Without a shared environmental memory, these rates should only depend on the effective diffusion coefficients of the species involved⁴⁷. The larger the effective diffusion coefficient, the faster the rate of group formation and growth, leading to larger groups within the same time interval. Nonetheless, our experimental results suggest that the effective diffusion coefficients decrease with ρ_p (Supplementary Fig. 2), so the augmented group formation for intermediate values of ρ_p must result from the presence of spatial correlations in the environment that increase the chances for particles to meet, i.e., the reuse of transient paths highlighted in Fig. 1 and Supplementary Fig. 1.

By calculating the effective rate coefficients (α_{mm} , α_{mg} and α_{gg}) from the simulated data, we can assess the relative importance of monomer–monomer, monomer–group and group–group aggregation on the kinetics of group formation (Fig. 5d). Both α_{mg} and α_{gg} present a maximum for intermediate values of ρ_p when group formation is enhanced, while α_{mm} is roughly constant in comparison. In the presence of passive particles, although monomer–monomer aggregation is key for the formation of the initial groups, the kinetics are dominated by groups catalysing their own growth through the addition of new monomers and merging with other existing groups. These aggregation events mediated by the presence of the shared environmental memory are hence behind the enhanced group formation observed at intermediate ρ_p . Indeed, when the aligning torque is switched off in simulation (Fig. 5e), the shared memory and stigmergy cannot develop (Fig. 4), resulting in aggregation rates that decay monotonically with increasing values of ρ_p , as one would expect when an increased number of obstacles hinders diffusion (Supplementary Fig. 2).

Discussion

In summary, our results demonstrate how, in a decentralised system composed of clueless active units with no explicit signalling pathway or information-processing capability, a dynamic environment can create the conditions for the emergence of a shared environmental memory that can coordinate and shape the system's collective response. Hence, confinement by crowding becomes a condition sufficient for self-organisation to emerge and to activate the system's coordination capabilities (e.g., by naturally evolving to larger groups)⁴⁸. In our experiments, the physical mechanism behind the emergence of these population dynamics is the aligning torque acting on the Janus particles due to the asymmetric demixing of the water–2,6-lutidine critical mixture caused by the presence of the non-fixed obstacles. Other physical mechanisms (e.g., electrostatic interactions, phoretic interactions, hydrodynamic coupling³⁹ or, even, sensory perception^{32,48}) can be expected to lead to the emergence of a shared field memory in other systems, which could also be reproduced in a coarse-grained manner by introducing an effective aligning torque in their motion dynamics. Indeed, similar mechanisms of shared memory which are primarily promoted and reinforced by dynamic environmental factors could also contribute to shaping the collective dynamics of other decentralised systems where individuals can instead actively signal to each other²⁷, such as communities of micro-organisms^{2,29}, social insects^{3,31} and robotic swarms^{4,7}. The feedback from the environment could then lower the threshold for quorum formation in natural communities³ and for reaching consensus in decision-making processes²⁶, e.g., by synergistically catalysing any pathway of explicit communication. Finally, we envisage that shared memories promoted by environmental dynamic features could become design factors to implement low-level rules to drive high-level self-organisation in artificial systems, including in the design of antimicrobial surfaces, of crowd management control tools, and of neuromorphic computers and artificial swarm intelligence⁴⁸.

Methods

Materials

Glass microscopy slides (Thermo Fisher) were purchased from VWR while glass coverslips were purchased from Thorlabs. The following chemicals were purchased and used as received: 2,6-lutidine ($\geq 99\%$, Sigma-Aldrich), acetone ($\geq 99.8\%$, Sigma-Aldrich), ethanol ($\geq 99.8\%$, Fisher Scientific), sodium hydroxide (NaOH, Fisher Scientific). Deionised (DI) water ($\geq 18 \text{ M}\Omega\cdot\text{cm}$) was collected from a Milli-Q purification system. Aqueous colloidal dispersions (5% w/v) of silica (SiO_2) colloids for sample preparation ($4.77 \pm 0.20 \mu\text{m}$ in diameter for Janus particle fabrication and as passive colloids; $7.00 \pm 0.15 \mu\text{m}$ in diameter as spacers) were purchased from Microparticles GmbH. Carbon rods of length 300 mm and diameter 6.15 mm for coating Janus particles by sputtering were purchased from Agar Scientific and cut to a length of 50 mm before use. Lens tissue for slide cleaning was purchased from Thorlabs. UV cure adhesive (Blufixx) and hydrophobic coating (RainX) for sample preparation were purchased from an online retailer (Amazon).

Slide cleaning protocol

Before their use for sample preparation, glass slides and coverslips were cleaned by wiping them with acetone-soaked lens tissue. RainX (a commercial solution which renders glass surfaces more hydrophobic and aids in limiting particles sticking to the glass chamber) was then smeared on both with a cotton bud and gently dried with a nitrogen gun. After 2 min, excess RainX was removed by wiping with acetone-soaked lens tissue. Glass slides for the deposition of colloidal monolayers were instead cleaned by sonication for 10 min in a 2 M NaOH ethanolic solution followed by three cycles of 5 min sonication in DI water. To dry them, the slides were withdrawn from water in the

presence of ethanol vapour (Marangoni drying) and, subsequently, blown dry with a nitrogen gun.

Fabrication of Janus particles

The Janus particles used in our experiments were fabricated from SiO_2 colloids of diameter $d = 4.77 \pm 0.20 \mu\text{m}$, which were coated on one side with a thin layer ($\approx 60 \text{ nm}$) of carbon. We first deposited a monolayer of colloids on a clean glass slide. The monolayer was obtained by evaporating a 40 μL droplet containing a 2.5% w/v dispersion of the colloids in DI water. The particles were then coated with a 60 nm thick carbon layer using an automatic carbon coater (AGB7367A, Agar Scientific). The thickness of the carbon layer was confirmed by atomic force measurements (AFM). Post-coating sonication allowed us to dislodge the half-coated particles in DI water from the glass slide to use them for sample preparation.

Sample preparation

Samples were prepared in the form of a quasi-two-dimensional glass chamber filled with a colloidal dispersion in a critical mixture of water–2,6-lutidine. Typical colloidal dispersions include Janus particles as well as passive SiO_2 particles and spacers. For example, to achieve a typical dispersion with densities of $\rho_a = 0.5\%$ and $\rho_p = 12.5\%$, we mixed stock dispersions of the three types of particles in DI water to achieve an aqueous dispersion containing 0.13% w/v of Janus particles, 5% w/v of passive particles and 0.08% w/v of spacers. This concentration of spacers was chosen to minimise their number in the field of view, whilst giving enough support to maintain the quasi-two-dimensional chamber's geometry. Samples with other densities (ρ_a and ρ_p) were obtained by linearly scaling these concentrations of Janus particles and passive particles to obtain the right values of ρ_a and ρ_p . Before their use, the colloidal mixtures were centrifuged at $1000 \times g$ for 3 min leaving a pellet; the supernatant was then removed and replaced with a 28.6% w/v water–2,6-lutidine solution. This process was repeated three times to remove residual DI water from the initial dispersion. Experiment-ready quasi-two-dimensional sample chambers containing a dispersion of colloids in a critical water–2,6-lutidine solution were prepared by sandwiching 10 μL of this final dispersion between a clean glass slide and a thin coverslip. The chamber was sealed by applying an ultraviolet-curable adhesive around the edges of the coverslip, which was then exposed to ultraviolet (UV) light for 30 s on each side. Before data acquisition, the sample was left to equilibrate over a 30-min period.

Optical setup and microscopy

All the experiments were performed on an inverted microscope (Leica, DMI4000) equipped with a homemade flow thermostat to maintain the critical suspension at a fixed temperature ($T = 30^\circ\text{C}$) below the critical point ($T_c \approx 34.1^\circ\text{C}$). The sample's field of view was illuminated at once with a green continuous-wave laser ($\lambda = 532 \text{ nm}$) at a power density of $2.5 \mu\text{W} \mu\text{m}^{-2}$ to simultaneously propel the Janus particles due to light absorption at the carbon cap³⁵. Both Janus and passive particles were tracked by digital video microscopy⁴⁹ using the image projected by a microscope objective ($\times 20$, $\text{NA} = 0.5$) on a monochrome complementary metal-oxide-semiconductor (CMOS) camera (Thorlabs, DCC1545M) with an acquisition rate of 10 frames per second. The incoherent illumination for the tracking is provided by a white-light-emitting diode (Thorlabs, MWWHLPI) directly projected onto the sample. A long-pass dichroic mirror (Thorlabs, DMLP605) with a 605-nm cut-on wavelength was used to combine laser and white light before the sample, while laser light was removed from the detection path with a notch filter centred at 532 nm (Semrock, NF01-532U-25).

Path revival function

To quantify the path reuse by the Janus particles, we define the path revival function $1 - C_{aa}(t)$, where $C_{aa}(t)$ is the cumulative probability that

a region crossed by an active particle will be crossed by another particle within a lag time τ . To compute $1 - C_{aa}(\tau)$ we define a circular region of diameter d around each active particle at a certain time t and measure how many of those regions have been crossed by the centre of another active particle up to lag time τ . If we consider the particles' velocities to be Poisson distributed when a path is chosen, then this function should follow an exponential distribution for persistent particles⁴¹

$$1 - C_{aa}(\tau) = \exp(-\tau/\tau_{\rho_p}), \quad (3)$$

where τ_{ρ_p} is the effective path revival lifetime, which we fit from the data. For both experiments and simulations, we assume that the initial positions in the particles' trajectories are uncorrelated (i.e., in the experiments, we only consider trajectories of individual particles before groups form and, in the simulations, the short-range attractive interaction between particles is turned off to prevent group formation).

Particle-based simulations

We consider a numerical model where n_a active spheres and n_p passive spheres of diameter d move inside a two-dimensional box of side $L = 60d$ with periodic boundary conditions. Both n_a and n_p are fixed to match the experimental values of ρ_a and ρ_p . As in the experiments, all particles, whether active or passive, have the same size d and mass m .

To map the simulations to the experiments, we consider the same Péclet number defined as,

$$Pe = \frac{dv}{D_t}, \quad (4)$$

where $d = 4.77 \mu\text{m}$, $v = 1.9 \mu\text{m s}^{-1}$, and $D_t = 0.0249 \mu\text{m}^2 \text{s}^{-1}$. Both velocity v and diameter d of the active particles were used to convert the reduced units in simulations to SI units. The translational diffusion coefficient D_t was calculated as

$$D_t = \frac{k_B T}{\gamma'}, \quad (5)$$

where k_B is the Boltzmann constant, T the absolute temperature, and γ' is the corrected translational drag coefficient for colloids at distance s from a surface⁵⁰, given by

$$\gamma' = \frac{\gamma}{1 - (9/16)(d/2s) + (1/8)(d/2s)^3}, \quad (6)$$

with

$$\gamma = 3\pi\mu d, \quad (7)$$

where μ is the fluid viscosity. We assume $2s = d$, $T = 303 \text{K}$, and $\mu = 2.1 \times 10^{-3} \text{Pa s}$ for the water–2,6-lutidine mixture. Similarly, the rotational diffusion coefficient D_r was calculated as

$$D_r = \frac{k_B T}{\beta'}, \quad (8)$$

where β' is the corrected rotational drag coefficient for colloids at distance s from a surface⁵⁰, given by

$$\beta' = \frac{\beta}{1 - (1/8)(d/2s)^3}, \quad (9)$$

with

$$\beta = \pi\mu d^3. \quad (10)$$

The trajectories of both active and passive particles were obtained by integrating their equations of motion using a velocity Verlet scheme implemented in the large-scale atomic/molecular massively parallel simulator (LAMMPS)⁵¹. Specifically, the particles' translational motion and rotational motion around one single axis (perpendicular to the simulation plane) are respectively described by the following Langevin equations,

$$m\dot{\mathbf{v}}_i(t) = -\nabla_{\mathbf{r}_i} V_i - \frac{m}{\tau_y} \mathbf{v}_i(t) + \sqrt{\frac{2mk_B T}{\tau_y}} \boldsymbol{\xi}_t^i(t) + F_a \hat{\mathbf{u}}_i(t) \quad (11)$$

and

$$I\dot{\omega}_i(t) = \Omega_i - \frac{\alpha I}{\tau_y} \omega_i(t) + \sqrt{\frac{2\alpha I k_B T}{\tau_y}} \xi_r^i(t), \quad (12)$$

where \mathbf{v}_i and ω_i are the translational and angular velocity for particle i , $\hat{\mathbf{u}}_i = (\cos \theta_i, \sin \theta_i)$, $\omega_i = \dot{\theta}_i$, F_a is the strength of the self-propulsion force for the active particles, τ_y is the damping time, I is the particles' inertia of rotation, V_i is the potential due to the interaction with all surrounding particles, and Ω_i is an effective torque due to the interaction of particle i with the surrounding passive particles. $\xi_t^i(t)$ and $\xi_r^i(t)$ are stochastic terms taken from a truncated random distribution of zero mean and unitary standard deviation⁵². Moreover, α is a model parameter that defines the relationship between the rotational (D_r) and translational (D_t) diffusion coefficients as

$$\frac{D_r}{D_t} = \alpha \frac{I}{m}. \quad (13)$$

where α is adjusted to map the experimental relation between D_t and D_r .

The motion of the passive particles is only governed by Eq. (11) (where we set $F_a = 0$) for computational efficiency as the rotational degree of freedom of the passive particles does not influence the numerical dynamics in the overdamped regime.

The interaction between particles is implemented with a Lennard-Jones potential given by

$$V_i = \sum_j V_{ij}(r_{ij}) = \sum_j 4\epsilon_{LJ} \left[\left(\frac{\sigma_{LJ}}{r_{ij}} \right)^{12} - \left(\frac{\sigma_{LJ}}{r_{ij}} \right)^6 \right], \quad (14)$$

where $r_{ij} = \|\mathbf{r}_i - \mathbf{r}_j\|$ is the distance between two particles, ϵ_{LJ} the depth of the potential well, and σ_{LJ} the width of the potential (distance at which the potential is zero). For passive particles, with purely repulsive interactions, we consider a truncated Lennard-Jones potential where the cut-off is set at $r_{\text{cut}} = d = 2^{1/6}\sigma_{LJ}$ to remove the attractive part. For active particles, we consider an attractive interaction with a cut-off set at $r_{\text{cut}} = 5d$. The depth of the potential well ϵ_{LJ} is obtained from experimental data (Supplementary Fig. 4).

Finally, to describe the impact of the passive particles on the rotational degrees of freedom of the active particles, we introduce the effective torque Ω_i on particle i ⁴³

$$\Omega_i = -\Omega_0 d^2 \hat{\mathbf{v}}_i \times \sum_{j=1}^{n_p} \nabla_{\mathbf{r}} \frac{e^{-\kappa r_{ij}}}{r_{ij}}, \quad (15)$$

where Ω_0 sets the strength of the torque, $\hat{\mathbf{v}}_i = \mathbf{v}_i / \|\mathbf{v}_i\|$ and \times is the cross product. The negative sign indicates that active particles steer away from the surrounding passive ones; $\kappa = 0.25/d$ gives the screening number in agreement with the range of experimental values estimated in⁴³. For numerical efficiency, we set a cut-off radius of four particle

diameters, where the value of the torque is much lower than the typical thermal noise. The torque used to map the experiments ($\Omega_0 = 72 \pm 16 k_B T$) was computed and confirmed from two different experimental measurements (Figs. 4a,c). In our simulations, the interactions of the active particles with the passive obstacles are therefore dependent on both the potential V_i and the torque Ω_i , while the interaction between active particles only depends on V_i as, working at low densities of active particles, they primarily interact when in groups.

Rate equations

The relevant mechanisms for the dynamics are (1) the formation of new groups by combining two free active particles (monomers); (2) the growth of a group by the addition of a monomer; (3) the pairwise merging of groups; and (4) their fragmentation. In the experiments, we define groups as clusters of size larger than two as dimers are unstable in time. Here, for completeness, we consider all cases. We assume that groups only lose one active particle at a time (fragmentation).

We define c_1 and c_i as the number densities of free active particles (monomers) and groups of size $i > 1$, respectively. The following rate equations then give the time evolution of c_1 ,

$$\dot{c}_1 = -\alpha_{mm}c_1^2 - \alpha_{mg}c_1 \sum_{j>1} c_j + \sum_{j>1} f_j c_j + f_2 c_2, \quad (16)$$

where the first term accounts for the formation of new groups, the second one for the growth of an existing group, the third for fragmentation, and the additional fourth term for the second free active particle released from the fragmentation of groups of size two. If the distance between groups is larger than the persistence length of the free active particles, the main mechanism of mass transport is diffusion and, in the absence of spatial correlations, the rates α_{mm} and α_{mg} should only depend on the size of the active particles and on their effective diffusion coefficients⁴⁷. For simplicity, we also consider that α_{mg} does not depend on the group size.

Similarly, for groups of size two,

$$\dot{c}_2 = \frac{\alpha_{mm}}{2}c_1^2 - \alpha_{mg}c_1c_2 - \alpha_{gg}c_2 \sum_{j>1} c_j - f_2c_2 + f_3c_3, \quad (17)$$

and for groups of size k ,

$$\dot{c}_k = \alpha_{mg}c_1c_{k-1} - \alpha_{mg}c_1c_k + \frac{1}{2}\alpha_{gg} \sum_{i+j=k} c_i c_j - \alpha_{gg}c_k \sum_{j>1} c_j + f_{k+1}c_{k+1} - f_k c_k. \quad (18)$$

If we now define the number density of groups $c_g = \sum_{j>1} c_j$ and the total fragmentation rate $f = \sum_{j>1} f_j c_j$, we obtain,

$$\dot{c}_1 = -\alpha_{mm}c_1^2 - \alpha_{mg}c_1c_g + f + f_2c_2, \quad (19)$$

and,

$$\dot{c}_g = \frac{\alpha_{mm}}{2}c_1^2 - \frac{\alpha_{gg}}{2}c_g^2 - f_2c_2. \quad (20)$$

In the simulation, we observe that the total fragmentation rate is constant for a large range of ρ_p up to the intermediate values where the largest groups are observed and then drops fast at higher values (Supplementary Fig. 5). Thus, aggregation rather than fragmentation is the leading factor in the non-monotonic dynamics of group formation observed in Fig. 2. If we neglect fragmentation, we obtain Eqs. (1) and (2), respectively.

Data availability

All data supporting the findings of this study are available in the manuscript, the Supplementary Information and in the Source Data file. Source data are provided with this paper.

Code availability

The code that supports the findings of this study is available from the corresponding authors on request.

References

- Vicsek, T. & Zafeiris, A. Collective motion. *Phys. Rep.* **517**, 71–140 (2012).
- Mukherjee, S. & Bassler, B. L. Bacterial quorum sensing in complex and dynamically changing environments. *Nat. Rev. Microbiol.* **17**, 371–382 (2019).
- Czaczkes, T. J., Grüter, C. & Ratnieks, F. L. Trail pheromones: an integrative view of their role in social insect colony organization. *Annu. Rev. Entomol.* **60**, 581–599 (2015).
- Moussaid, M., Garnier, S., Theraulaz, G. & Helbing, D. Collective information processing and pattern formation in swarms, flocks, and crowds. *Top. Cogn. Sci.* **1**, 469–497 (2009).
- Sieben, A., Schumann, J. & Seyfried, A. Collective phenomena in crowds—where pedestrian dynamics need social psychology. *PLoS ONE* **12**, e0177328 (2017).
- Bechinger, C. et al. Active particles in complex and crowded environments. *Rev. Mod. Phys.* **88**, 045006 (2016).
- Dorigo, M., Theraulaz, G. & Trianni, V. Reflections on the future of swarm robotics. *Sci. Robot.* **5**, eabe4385 (2020).
- Palacci, J., Sacanna, S., Steinberg, A. P., Pine, D. J. & Chaikin, P. M. Living crystals of light-activated colloidal surfers. *Science* **339**, 936–940 (2013).
- Lavergne, F. A., Wendehenne, H., Bäuerle, T. & Bechinger, C. Group formation and cohesion of active particles with visual perception-dependent motility. *Science* **364**, 70–74 (2019).
- Buttinoni, I. et al. Dynamical clustering and phase separation in suspensions of self-propelled colloidal particles. *Phys. Rev. Lett.* **110**, 238301 (2013).
- Cates, M. E. & Tailleur, J. Motility-induced phase separation. *Annu. Rev. Condens. Matter Phys.* **6**, 219–244 (2015).
- Ginot, F., Theurkauff, I., Detcheverry, F., Ybert, C. & Cottin-Bizonne, C. Aggregation-fragmentation and individual dynamics of active clusters. *Nat. Commun.* **9**, 696 (2018).
- Bricard, A., Caussin, J.-B., Desreumaux, N., Dauchot, O. & Bartolo, D. Emergence of macroscopic directed motion in populations of motile colloids. *Nature* **503**, 95–98 (2013).
- Yan, J. et al. Reconfiguring active particles by electrostatic imbalance. *Nat. Mater.* **15**, 1095–1099 (2016).
- Pinçe, E. et al. Disorder-mediated crowd control in an active matter system. *Nat. Commun.* **7**, 10907 (2016).
- Khadka, U., Holubec, V., Yang, H. & Cichos, F. Active particles bound by information flows. *Nat. Commun.* **9**, 3864 (2018).
- Reichhardt, C. & Reichhardt, C. O. Local melting and drag for a particle driven through a colloidal crystal. *Phys. Rev. Lett.* **92**, 108301 (2004).
- Kümmel, F., Shabestari, P., Lozano, C., Volpe, G. & Bechinger, C. Formation, compression and surface melting of colloidal clusters by active particles. *Soft Matter* **11**, 6187–6191 (2015).
- Van Der Meer, B., Fillion, L. & Dijkstra, M. Fabricating large two-dimensional single colloidal crystals by doping with active particles. *Soft Matter* **12**, 3406–3411 (2016).
- Omar, A. K., Wu, Y., Wang, Z.-G. & Brady, J. F. Swimming to stability: structural and dynamical control via active doping. *ACS Nano* **13**, 560–572 (2018).
- Dietrich, K. et al. Active atoms and interstitials in two-dimensional colloidal crystals. *Phys. Rev. Lett.* **120**, 268004 (2018).

22. Ramanarivo, S., Ducrot, E. & Palacci, J. Activity-controlled annealing of colloidal monolayers. *Nat. Commun.* **10**, 3380 (2019).
23. Banerjee, J. P., Mandal, R., Banerjee, D. S., Thutupalli, S. & Rao, M. Unjamming and emergent nonreciprocity in active ploughing through a compressible viscoelastic fluid. *Nat. Commun.* **13**, 4533 (2022).
24. Madden, I. P., Wang, L., Simmchen, J. & Luijten, E. Hydrodynamically controlled self-organization in mixtures of active and passive colloids. *Small* **18**, 2107023 (2022).
25. Trivedi, M., Saxena, D., Ng, W. K., Sapienza, R. & Volpe, G. Self-organized lasers from reconfigurable colloidal assemblies. *Nat. Phys.* **18**, 939–944 (2022).
26. Garnier, S., Gautrais, J. & Theraulaz, G. The biological principles of swarm intelligence. *Swarm Intell.* **1**, 3–31 (2007).
27. Marsh, L. & Onof, C. Stigmergic epistemology, stigmergic cognition. *Cogn. Syst. Res.* **9**, 136–149 (2008).
28. Lugano, R., Ramachandran, M. & Dimberg, A. Tumor angiogenesis: causes, consequences, challenges and opportunities. *Cell. Mol. Life Sci.* **77**, 1745–1770 (2020).
29. Phan, T. V. et al. Bacterial route finding and collective escape in mazes and fractals. *Phys. Rev. X* **10**, 031017 (2020).
30. Tweedy, L. et al. Seeing around corners: Cells solve mazes and respond at a distance using attractant breakdown. *Science* **369**, eaay9792 (2020).
31. Reid, C. R., Sumpter, D. J. T. & Beekman, M. Optimisation in a natural system: Argentine ants solve the Towers of Hanoi. *J. Exp. Biol.* **214**, 50–58 (2011).
32. Murakami, H., Feliciani, C., Nishiyama, Y. & Nishinari, K. Mutual anticipation can contribute to self-organization in human crowds. *Sci. Adv.* **7**, eabe7758 (2021).
33. Werfel, J., Petersen, K. & Nagpal, R. Designing collective behavior in a termite-inspired robot construction team. *Science* **343**, 754–758 (2014).
34. Nakayama, B. et al. Tunable pheromone interactions among microswimmers. *Proc. Natl. Acad. Sci. USA* **120**, e2213713120 (2023).
35. Buttinoni, I., Volpe, G., Kümmel, F., Volpe, G. & Bechinger, C. Active brownian motion tunable by light. *J. Phys. Condens. Matter* **24**, 284129 (2012).
36. Huang, R. et al. Direct observation of the full transition from ballistic to diffusive brownian motion in a liquid. *Nat. Phys.* **7**, 576–580 (2011).
37. Pesce, G., Volpe, G., Volpe, G. & Sasso, A. Long-term influence of fluid inertia on the diffusion of a brownian particle. *Phys. Rev. E* **90**, 042309 (2014).
38. Mognetti, B. M. et al. Living clusters and crystals from low-density suspensions of active colloids. *Phys. Rev. Lett.* **111**, 245702 (2013).
39. Das, S. et al. Boundaries can steer active janus spheres. *Nat. Commun.* **6**, 8999 (2015).
40. Simmchen, J. et al. Topographical pathways guide chemical microswimmers. *Nat. Commun.* **7**, 10598 (2016).
41. Enns, E., Smith, B. & Ehlers, P. Hitting spheres by straight-line motion or brownian motion. *J. Appl. Probab.* **21**, 70–79 (1984).
42. Gomez-Solano, J. R. et al. Tuning the motility and directionality of self-propelled colloids. *Sci. Rep.* **7**, 14891 (2017).
43. Liebchen, B. & Löwen, H. Which interactions dominate in active colloids? *J. Chem. Phys.* **150**, 061102 (2019).
44. Ašperger, S. & Ašperger, S. *Chemical Kinetics and Reaction Mechanisms. Chemical Kinetics and Inorganic Reaction Mechanisms*. 3–103 (Springer, 2003).
45. Brambilla, M., Ferrante, E., Birattari, M. & Dorigo, M. Swarm robotics: a review from the swarm engineering perspective. *Swarm Intell.* **7**, 1–41 (2013).
46. Hamann, H. & Reina, A. Scalability in computing and robotics. *IEEE Trans. Comput.* **71**, 1453–1465 (2021).
47. Krapivsky, P. L., Redner, S. & Ben-Naim, E. *A Kinetic View of Statistical Physics*. (Cambridge University Press, 2010).
48. Araújo, N. A. M. et al. Steering self-organisation through confinement. *Soft Matter* **19**, 1695–1704 (2023).
49. Crocker, J. C. & Grier, D. G. Methods of digital video microscopy for colloidal studies. *J. Colloid Interface Sci.* **179**, 298–310 (1996).
50. Leach, J. et al. Comparison of Faxén’s correction for a microsphere translating or rotating near a surface. *Phys. Rev. E* **79**, 026301 (2009).
51. Plimpton, S. Fast parallel algorithms for short-range Molecular Dynamics. *J. Comp. Phys.* **117**, 1–19 (1995).
52. Dunweg, B. & Wolfgang, P. Brownian Dynamics without gaussian random numbers. *Int. J. Mod. Phys. C* **2**, 817–827 (1991).

Acknowledgements

We are grateful to Samantha Rueber and Matthew Blunt for initial training on experimental techniques. C.S.D. and N.A.M.A. acknowledge financial support from the Portuguese Foundation for Science and Technology (FCT) under Contracts no. PTDC/FIS-MAC/5689/2020, EXPL/FIS-MAC/0406/2021, CEECIND/00586/2017, UIDB/00618/2020, and UIDP/00618/2020. G.V. (Giovanni) acknowledges funding from the Horizon Europe ERC Consolidator Grant MAPEI (Grant No. 101001267) and the Knut and Alice Wallenberg Foundation (Grant No. 2019.0079). G.V. (Giorgio) acknowledges sponsorship for this work by the US Office of Naval Research Global (Award No. N62909-18-1-2170). N.A.M.A. and G.V. (Giorgio) acknowledge support from the UCL MAPS Faculty Visiting Fellowship programme.

Author contributions

Author contributions are defined based on the CRediT (Contributor Roles Taxonomy) and listed alphabetically. Conceptualisation: G.V. (Giovanni), N.A.M.A., G.V. (Giorgio). Data curation: C.S.D., M.T. Formal analysis: C.S.D., M.T., N.A.M.A., G.V. (Giorgio). Funding acquisition: G.V. (Giorgio). Investigation: C.S.D., M.T., N.A.M.A. Methodology: C.S.D., M.T., G.V. (Giovanni), N.A.M.A., G.V. (Giorgio). Project administration: G.V. (Giorgio). Resources: N.A.M.A., G.V. (Giorgio). Software: C.S.D. Supervision: C.S.D., N.A.M.A., G.V. (Giorgio). Validation: C.S.D., M.T., G.V. (Giorgio). Visualisation: C.S.D., M.T., G.V. (Giorgio). Writing—original draft: C.S.D., G.V. (Giovanni), N.A.M.A., G.V. (Giorgio). Writing—review and editing: C.S.D., M.T., G.V. (Giovanni), N.A.M.A., G.V. (Giorgio).

Funding

Open access funding provided by University of Gothenburg.

Competing interests

The authors declare no competing interests.

Additional information

Supplementary information The online version contains supplementary material available at <https://doi.org/10.1038/s41467-023-43099-0>.

Correspondence and requests for materials should be addressed to Giovanni Volpe, Nuno A. M. Araújo or Giorgio Volpe.

Peer review information *Nature Communications* thanks the anonymous reviewers for their contribution to the peer review of this work. A peer review file is available.

Reprints and permissions information is available at <http://www.nature.com/reprints>

Publisher’s note Springer Nature remains neutral with regard to jurisdictional claims in published maps and institutional affiliations.

Open Access This article is licensed under a Creative Commons Attribution 4.0 International License, which permits use, sharing, adaptation, distribution and reproduction in any medium or format, as long as you give appropriate credit to the original author(s) and the source, provide a link to the Creative Commons license, and indicate if changes were made. The images or other third party material in this article are included in the article's Creative Commons license, unless indicated otherwise in a credit line to the material. If material is not included in the article's Creative Commons license and your intended use is not permitted by statutory regulation or exceeds the permitted use, you will need to obtain permission directly from the copyright holder. To view a copy of this license, visit <http://creativecommons.org/licenses/by/4.0/>.

© The Author(s) 2023